Two-step (analytical + geostatistical) pre-stack seismic inversion for elastic properties estimation and litho-fluid facies classification

M. ALEARDI

Earth Sciences Department, University of Pisa, Italy

ABSTRACT   We infer the P-wave velocity, S-wave velocity, density, and the litho-fluid classes through a two cascade estimation steps. First, we analytically invert each seismic gather independently using a linear 1D convolutional forward operator and assuming a Gaussian-mixture prior. This step is computationally fast because no hard or lateral constraints are imposed to the recovered solution. The outcomes provided by the analytical inversion are used as auxiliary variables for a geostatistical simulation that generates the initial ensemble of models for the subsequent stage of geostatistical inversion in which the estimated models are generated and iteratively updated according to a more realistic non-parametric prior, while spatial and hard constraints are now imposed to the solution. This second step determines the model update from the match between observed and predicted seismic gathers that are computed through a 1D convolutional operator based on the full Zoeppritz equations. Synthetic inversions are used to validate the method and demonstrate that starting the second inversion step from an ensemble of models that already quite accurately reproduce the observed data allows for a fast retrieval of a subsurface model that honours the non-parametric prior, the hard constraints, and the spatial continuity patterns as coded by the variogram model.

Key words: reflection seismic, inversion, amplitude versus angle.

1. Introduction

Seismic inversion aims to describe the spatial variability of elastic properties and litho-fluid facies around the study area. The inversion process simultaneously estimates discrete (i.e. litho-fluid facies) and continuous (e.g. elastic properties) model parameters from the observed pre-stack seismic data [partially stacked data at different incidence angles: Gunning and Sams (2018)]. To limit the computational cost of the inversion procedure linearisations of the exact Zoeppritz equations are often employed as the seismic forward modelling, although it is known that these linearisations are not capable of predicting the reflected amplitudes at far source-receiver offsets and when significant elastic contrasts at the reflecting interfaces occur. One of the most popular linear inversion approach is that proposed by Buland and Omre (2003) that infers the elastic property of P-wave velocity (Vp), S-wave velocity (Vs), and density (ρ) and the associated uncertainties under the assumptions of Gaussian distributed noise and log-Gaussian distributed elastic parameters. The Gaussian

assumption is often employed because it allows for an analytical and computationally fast derivation of the predicted model and associated uncertainties (Tarantola, 2005). However, it is known that the Gaussian model usually oversimplifies the actual distribution of the reservoir parameters in the subsurface because it neglects the influence exerted by the litho-fluid facies. From a mathematical point of view, this means that a Gaussian model does not capture the multimodality of the actual distribution of elastic parameters and that more complex distributions are needed such as Gaussian mixture or even non-parametric distributions (Aleardi *et al.*, 2018).

Seismic reservoir characterisation is an ill-posed problem and for this reason, regularisation strategies are usually introduced into the inversion framework (Aleardi, 2015; Aster *et al.*, 2018; Menke, 2018). The regularisation terms force the final prediction to honour some desired statistical or structural characteristics, thus limiting the number of subsurface models that equally fit the observed data. In practice, soft and hard model constraints exist. Hard constraints are required to be satisfied by the predicted model and are usually defined by well log data recorded in the investigated area. Soft constraints are introduced as additional terms in the misfit function and penalise models that although producing good data predictions, do not honour the desired characteristics of the solution. Both types of constraints are often infused into pre-stack seismic inversion and some examples can be found in Tetyukhina *et al.* (2010), Theune *et al.* (2010), Ulvmoen *et al.* (2010), Alemie and Sacchi (2011), Bongajum *et al.* (2013), Aleardi *et al.* (2015, 2019), Zunino *et al.* (2015), Wang and Wang (2016), She *et al.* (2018), Aleardi and Salusti (2019). Geostatistical inversion is a popular approach to include spatial constraints into the estimation process, in which geostatistical techniques generate subsurface models that satisfy the imposed constraints. Then, these models are updated according to their match with the observed seismic response and this process is iterated until a certain condition (i.e. a previously selected data misfit value) is satisfied. The first applications of this approach to seismic inversion can be found in Bortoli *et al.* (1993) and Hass and Dubrule (1994), while more recent developments are described by Doyen (2007), Bosch *et al.* (2009), Azevedo and Soares (2017), and Laloy *et al.* (2018). One outstanding benefit of the geostatistical approach is that it does not need an analytical forward operator or Gaussian or multi-Gaussian assumptions about noise and model parameter distributions (Bosch *et al.*, 2010). However, due to the size of seismic data and the large number of subsurface realisations needed to reach convergence, this method can become computationally prohibitive, although the recent advent of high-speed multi-core CPUs and GPUs have significantly promoted its application to reservoir characterisation studies.

In this paper, we present an inversion strategy that combines a first step of analytical inversion with a subsequent geostatistical inversion. The first stage makes use of the Bayes' formalism and a linear approximation of the nonlinear Zoeppritz equations to infer litho-fluid facies and elastic properties together with the associated uncertainties from partially stacked seismic data. In this case, we assume Gaussian distributed noise in the data, and a Gaussian-mixture distribution for the model properties, so that the posterior uncertainties can be expressed in a closed-form. For computationally feasibility reasons, this step inverts each seismic gather independently, thus overlooking hard and lateral constraints, and only imposes a vertical correlation model to preserve the temporal continuity of the solution. These characteristics, together with the analytical prior model and the linear forward operator, make this first inversion step extremely fast. The second inversion stage is aimed at imposing hard and spatial constraints and at refining the outcomes of the first

step according to a more realistic non-parametric prior model. More in detail, the models generated according to the posterior distribution estimated in the first step are used as auxiliary variables in a geostatistical simulation process that generates the initial ensemble of candidate solutions. This initial population is refined during the iterative second step of geostatistical inversion to properly reproduce the observed data. Differently from the analytical inversion, now we employ the exact non-linear Zoeppritz equations as the forward modelling and we assume a non-parametric prior for the continuous property, thus relaxing the assumption of an analytical *a-priori* model. Note that in the first inversion step the posterior facies model can be analytically computed, while a numerical method is used for the facies classification in the geostatistical inversion. Here we employ the Bayes classification method but if needed more sophisticated machine learning algorithms can be employed (e.g. random forest, support vector classifiers, neural networks). For the lack of available field data, we validate the implemented approach on synthetic seismic gathers generated from a realistic subsurface model and assuming different signal-to-noise ratios.

2. Methods

2.1. First step: linear inversion

In the first inversion step the relation between the model parameters and the data is expressed by a linear approximation of the full Zoeppritz equations (Aki and Richards, 1980):

$$Rpp(t,\theta) = \frac{1}{2}(1 + tan^2(\theta))\frac{\partial}{\partial t}\ln Vp(t) + 4\frac{\overline{Vs}^2(t)}{\overline{Vp}^2(t)}sin^2(\theta)\frac{\partial}{\partial t}\ln Vs(t)$$

$$+ \frac{1}{2}\left(1 - 4\frac{\overline{Vs}^2(t)}{\overline{Vp}^2(t)}sin^2(\theta)\right)\frac{\partial}{\partial t}\ln\rho(t)$$

$$= \alpha_{Vp}\frac{\partial}{\partial t}\ln Vp(t) + \alpha_{Vs}\frac{\partial}{\partial t}\ln Vs(t) + \alpha_{\rho}\frac{\partial}{\partial t}\ln\rho(t), \tag{1}$$

where *Rpp* is the P-wave reflection coefficient, *t* is the time, θ is the incidence angle, whereas $\frac{\overline{Vs}^2}{\overline{Vp}^2}$ indicates the average *Vs/Vp* ratio at the reflecting interfaces that can be derived, for example, from the so-called low-frequency elastic back-ground model usually estimated from well log data interpolation. In matrix notation and adopting a convolutional forward modelling, the seismic gather **d** can be computed as follows:

$$\mathbf{d} = \mathbf{SADe} = \mathbf{Ge}, \tag{2}$$

where **S** is the wavelet matrix, **A** contains the numerical coefficients $\alpha_{Vp}(t)$, $\alpha_{Vs}(t)$, and $\alpha_{\rho}(t)$ of Eq. 1, **D** expresses the first-order numerical derivative operator and contains discrete time samples of the natural logarithm of *Vp*, *Vs*, and *ρ*, whereas the **G** matrix constitutes the linear forward

operator. We assume a Gaussian-mixture prior for $\mathbf{e}$, that is we assume the natural logarithm of elastic parameters to be Gaussian-distributed within each litho-fluid facies. This prior model can be written as follows:

$$p(\mathbf{e}) = \sum_{k=1}^{K} \omega_i \mathcal{N}\left(\mathbf{e}; \boldsymbol{\mu}_{\mathbf{e}}^k, \boldsymbol{\Sigma}_{\mathbf{e}}^k\right), \quad (3)$$

where K is the total number of components of the Gaussian-mixture distribution (i.e. the number of facies considered), ω_i is the prior weight of the i-th component, $\mathcal{N}$ indicates the Gaussian distribution with mean vector $\boldsymbol{\mu}_{\mathbf{e}}^k$ and covariance matrix $\boldsymbol{\Sigma}_{\mathbf{e}}^k$, whereas the superscript k indicates that such mean and the covariance are facies dependent. The number of facies and the statistical properties of each Gaussian component can be determined from available well log data investigating the study area. Note that the coefficients ω_i define the *a-priori* probability of occurrence of the i-th facies. Given a linear forward operator, the posterior model is again a Gaussian mixture and is expressed by:

$$p(\mathbf{e}|\mathbf{d}, \mathbf{f}) = \sum_{k=1}^{K} \lambda_i \mathcal{N}\left(\mathbf{e}; \boldsymbol{\mu}_{\mathbf{e}|\mathbf{d},\mathbf{f}}^k, \boldsymbol{\Sigma}_{\mathbf{e}|\mathbf{d},\mathbf{f}}^k\right), \tag{4}$$

where $\mathbf{f}$ is the vector describing the low-frequency elastic back-ground model, whereas the posterior weights λ_i, and the a-posteriori mean vector and covariances matrix ($\boldsymbol{\mu}_{\mathbf{e}|\mathbf{d},\mathbf{f}}^k$ and $\boldsymbol{\Sigma}_{\mathbf{e}|\mathbf{d},\mathbf{f}}^k$, respectively) can be computed as follows (de Figueredo *et al.*, 2018):

$$\boldsymbol{\mu}_{\mathbf{e}|\mathbf{d},\mathbf{f}}^k = \boldsymbol{\mu}_{\mathbf{e}}^k + \begin{bmatrix} \boldsymbol{\Sigma}_{\mathbf{e}}^k \\ \mathbf{G}\boldsymbol{\Sigma}_{\mathbf{e}}^k \end{bmatrix} \begin{bmatrix} \boldsymbol{\Sigma}_{\mathbf{e}}^k + \boldsymbol{\Sigma}_{\mathbf{f}} & \boldsymbol{\Sigma}_{\mathbf{e}}^k \mathbf{G}^T \\ \boldsymbol{\Sigma}_{\mathbf{e}}^k \mathbf{G} & \mathbf{G}^T \boldsymbol{\Sigma}_{\mathbf{d}}^{-1} \mathbf{G} \end{bmatrix}^{-1} \left(\begin{bmatrix} \mathbf{f} \\ \mathbf{d} \end{bmatrix} - \begin{bmatrix} \boldsymbol{\mu}_{\mathbf{e}}^k \\ \mathbf{G}\boldsymbol{\mu}_{\mathbf{e}}^k \end{bmatrix} \right), \tag{5}$$

$$\boldsymbol{\Sigma}_{\mathbf{e}|\mathbf{d},\mathbf{f}}^k = \boldsymbol{\Sigma}_{\mathbf{e}}^k - \begin{bmatrix} \boldsymbol{\Sigma}_{\mathbf{e}}^k \\ \mathbf{G}\boldsymbol{\Sigma}_{\mathbf{e}}^k \end{bmatrix} \begin{bmatrix} \boldsymbol{\Sigma}_{\mathbf{e}}^k + \boldsymbol{\Sigma}_{\mathbf{f}} & \boldsymbol{\Sigma}_{\mathbf{e}}^k \mathbf{G}^T \\ \boldsymbol{\Sigma}_{\mathbf{e}}^k \mathbf{G} & \mathbf{G}^T \boldsymbol{\Sigma}_{\mathbf{d}}^{-1} \mathbf{G} \end{bmatrix}^{-1} \begin{bmatrix} \boldsymbol{\Sigma}_{\mathbf{e}}^k \\ \mathbf{G}\boldsymbol{\Sigma}_{\mathbf{e}}^k \end{bmatrix}^T, \tag{6}$$

$$p(\boldsymbol{\pi}|\mathbf{d}, \mathbf{f}) = \lambda_{\pi} = \frac{\omega_i N\left(\begin{bmatrix} \mathbf{f} \\ \mathbf{d} \end{bmatrix}; \begin{bmatrix} \boldsymbol{\mu}_{\mathbf{e}}^k \\ \mathbf{G}\boldsymbol{\mu}_{\mathbf{e}}^k \end{bmatrix}, \begin{bmatrix} \boldsymbol{\Sigma}_{\mathbf{e}}^k + \boldsymbol{\Sigma}_{\mathbf{f}} & \boldsymbol{\Sigma}_{\mathbf{e}}^k \mathbf{G}^T \\ \boldsymbol{\Sigma}_{\mathbf{e}}^k \mathbf{G} & \mathbf{G}^T \boldsymbol{\Sigma}_{\mathbf{d}}^{-1} \mathbf{G} \end{bmatrix} \right)}{\sum_{i=1}^{K} \omega_i N\left(\begin{bmatrix} \mathbf{f} \\ \mathbf{d} \end{bmatrix}; \begin{bmatrix} \boldsymbol{\mu}_{\mathbf{e}}^k \\ \mathbf{G}\boldsymbol{\mu}_{\mathbf{e}}^k \end{bmatrix}, \begin{bmatrix} \boldsymbol{\Sigma}_{\mathbf{e}}^k + \boldsymbol{\Sigma}_{\mathbf{f}} & \boldsymbol{\Sigma}_{\mathbf{e}}^k \mathbf{G}^T \\ \boldsymbol{\Sigma}_{\mathbf{e}}^k \mathbf{G} & \mathbf{G}^T \boldsymbol{\Sigma}_{\mathbf{d}}^{-1} \mathbf{G} \end{bmatrix} \right)}. \tag{7}$$

The symbol represents the facies class, the matrix $\boldsymbol{\Sigma}_{\mathbf{f}}$ represents the uncertainties in the assumed low-frequency model, and the coefficients λ_{π} are the point-wise posterior probability of facies, where point-wise means that the coefficients λ_{π} at each spatial position are independent from those estimated at the neighbouring positions. Finally, the *a-posteriori* mean elastic model can be derived as a weighted summation over the posterior Gaussian components:

$$\mathbf{e}_{est} = \sum_{k=1}^{K} \lambda_k \boldsymbol{\mu}_{\mathbf{e}|\mathbf{d},\mathbf{f}}^{k}. \tag{8}$$

Note that the prior model covariance matrix $\boldsymbol{\Sigma}_{\mathbf{e}}^{k}$ expresses both the mutual correlation of elastic properties and their vertical variability. The correlation is given by a stationary covariance matrix, while the vertical correlation is obtained by multiplying (Kronecker product) the stationary covariance matrix with a first-order exponential function expressing the vertical correlation model (Buland and Omre, 2003):

$$\tau = \exp\left(-\frac{\mathbf{h}^2}{\alpha^2}\right), \tag{9}$$

where $\mathbf{h}$ is the temporal axis of the autocorrelation function, and α is the parameter that defines the temporal dependency. As previously mentioned each seismic gather is inverted separately so that the posterior model $p(\mathbf{e}|\mathbf{d}, \mathbf{f})$ over the entire investigated area is only constrained by the *a-priori* information and by the vertical correlation model, but it does not honour any hard (e.g. well log) or lateral constraints.

2.2. Second step: geostatistical inversion

In this second step, we relax the assumption of a Gaussian mixture *a-priori* model and we more realistically assume a facies-dependent non-parametric distribution for the elastic properties. This non-parametric model can be derived by applying the kernel density estimation algorithm to the ensemble of available well log data. In this context, the first step of linear inversion aims to provide an initial, preliminary, solution under the assumption of a Gaussian-mixture prior. The second step of geostatistical inversion not only includes hard and the lateral constraints, but also refines the linear solution according to a more realistic distribution for the unknown parameters. The vector $\boldsymbol{\mu}_{\mathbf{e}|\mathbf{d},\mathbf{f}}^{k}$ and covariance matrix $\boldsymbol{\Sigma}_{\mathbf{e}|\mathbf{d},\mathbf{f}}^{k}$ estimated in the first inversion stage are, then, used to generate an ensemble of models from the posterior distribution that serve as auxiliary variables in the geostatistical simulation process that generates the ensemble of starting models for the subsequent inversion step. The aim is to generate starting models that are in accordance to the desired spatial correlation model, that honour both the *a-posteriori* model provided by the linear inversion and the available hard constraints, and that also preserve the desired mutual correlation between the simulated properties (correlation between *Vp*, *Vs,* and ρ in this case). However, this initial ensemble of models is not constrained by the seismic data, and for this reason, they are updated during the following geostatistical inversion to match the observed seismic gathers while still preserving all the desired soft and hard constraints as well as the mutual correlation between the model parameters. The outcomes of the second inversion step are predicted *Vp*, *Vs*, ρ, and facies models, together with an approximated quantification of the associated uncertainties.

Before running the geostatistical inversion, some preliminary steps are needed:

1a) exploit the available well log data [e.g. the data previously used to compute the

$p(\mathbf{e})$distribution], to numerically compute the joint distribution between *Vs* and *Vp* $p(Vs, Vp)$ and between ρ, *Vp*, and *Vs* $p(\rho, Vp, Vs)$. The kernel density estimation algorithm can be used. Such joint distributions are used in the geostatistical simulation process to preserve plausible correlations between the elastic parameters in all the simulated models. Note that the use of numerical distributions, instead of the linear correlation coefficients, guarantees the preservation of non-linear or heteroscedastic characteristics of the experimental joint distribution as estimated from well log data;

2a) define the variogram model expressing the assumed lateral variability of the elastic parameters to be included into the geostatistical simulation process (e.g. by the analysis of the lateral variability of the available seismic data);

3a) use the ensemble of available well log data to train the facies classification method employed in the geostatistical inversion. Here we use the well-known Bayes classification, but other more sophisticated approaches could be used as well;

4a) use the outcomes of the first step of linear inversion to generate an ensemble of Q facies, *Vp*, *Vs*, and ρ models $\{\boldsymbol{\pi}_1, \boldsymbol{\pi}_2, \ldots, \boldsymbol{\pi}_Q, \mathbf{Vp}_1, \mathbf{Vp}_2, \ldots, \mathbf{Vp}_Q, \mathbf{Vs}_1, \mathbf{Vs}_2, \ldots, \mathbf{Vs}_Q, \boldsymbol{\rho}_1, \boldsymbol{\rho}_2, \ldots, \boldsymbol{\rho}_Q\}$ according to the statistical properties of the posterior models $p(\boldsymbol{\pi} \,|\, \mathbf{d}\,, \mathbf{f}\,)$, and $p(\mathbf{e}|\mathbf{d}, \mathbf{f})$. In correspondence of the available well log data locations and for all the Q models, compute the correlation coefficients γ between the simulated properties and the borehole data, thus deriving $(\gamma_{Vp}^i, \gamma_{Vs}^i, \gamma_{\rho}^i)$, with i = 1, 2, …, Q. These correlation coefficients are used in the following co-simulation process to generate the ensemble of starting models for the geostatistical inversion. Note that a high γ_x^i value indicates that the *i*-th simulated property is in good agreement with the borehole information and assuming that the quality of this prediction is high even for the spatial locations away from well control, it is desirable that the *i*-th starting model to be generated is highly correlated with the considered posterior realisation. In the extreme case of a correlation coefficient equal to zero, the corresponding simulated model in the following co-simulation process will be only influenced by the *a-priori* information $p(\mathbf{e})$ and the hard constraints;

5a) include into the Q *Vp*, *Vs*, ρ and facies models generated in the previous step all the available hard data constraints (i.e. well log information). The so updated ensemble of models $\mathbf{M}= \{\boldsymbol{\pi}_1^{aux}, \boldsymbol{\pi}_2^{aux}, \ldots, \boldsymbol{\pi}_Q^{aux}, \mathbf{Vp}_1^{aux}, \mathbf{Vp}_2^{aux}, \ldots, \mathbf{Vp}_Q^{aux}, \mathbf{Vs}_1^{aux}, \mathbf{Vs}_2^{aux}, \ldots, \mathbf{Vs}_Q^{aux}, \boldsymbol{\rho}_1^{aux}, \boldsymbol{\rho}_2^{aux}, \ldots, \boldsymbol{\rho}_Q^{aux}\}$ that merges the posterior realisation and the hard data constraints, represents the auxiliary variables for the following simulation process.

After these preliminary operations, the initial ensemble of elastic models for the geostatistical inversion can be generated. The goal is to update the previously generated **M** elastic models according to the desired spatial continuity pattern. The steps advocated to this task are the following:

1b) generate the initial ensemble of Q *Vp* models with the Direct Sequential Co-Simulation (co-DSS) algorithm that reproduces both the global histogram and the variogram of a variable to be simulated by combining the collocated simple cokriging method with the normal score transformation (Soares, 2001). In our implementation the *i*-th $\mathbf{Vp}_i^{aux}$ model is used as an auxiliary variable while the

associated correlation coefficient γ_{Vp}^i is used, under the Markov-type assumption (Xu *et al.*, 1992), to compute the cross-covariance of the variable to be simulated given the previously determined auto-covariance of the auxiliary variable (Sarma, 2010). We start from the *Vp* because it is the best resolved parameter in a pre-stack seismic inversion. Let **Vp*** be the variable to be simulated over a 3-D grid $\boldsymbol{\Psi} = (\mathbf{x}, \mathbf{y}, \mathbf{z})$ with spatial coordinates expressed by the vectors **x**, **y**, and **z**, whereas $\boldsymbol{\psi_0}$ indicates the considered spatial location where the property must be simulated ($\boldsymbol{\psi_0} \in \boldsymbol{\Psi}$). The entire simulation is an iterative process that visits all the spatial locations defined by $\boldsymbol{\Psi}$. In each iteration, the simulated value is conditioned on the hard constraints and on the previously simulated values falling within a neighbourhood ensemble $\boldsymbol{\Psi_N}$ defined around $\boldsymbol{\psi_0}$. The co-simulation process is performed as usual. In particular, the autocovariance of the variable to be simulated is computed as:

$$C_{Vp^*}(\mathbf{h}) = \gamma_{Vp} \frac{\sigma_{Vp^*}}{\sigma_{Vp^{aux}}} C_{Vp}(\mathbf{h}) = \gamma_{Vp} C_{Vp}(\mathbf{h}) \tag{10}$$

where the symbol σ represents the standard deviation, the vector **h** represents the spatial Euclidean distance, C indicates the spatial covariance, C_{Vp_π} is the assumed covariance model for *Vp*, whereas the subscript π indicates that the covariance model is facies dependent. Note that $\frac{\sigma_{Vp^*}}{\sigma_{Vp^{aux}}} = 1$ because the assumed standard deviation of the auxiliary variable and of the variable to be simulated are equal (i.e. they both represent the *Vp* parameter). For notational convenience, in Eq. 10 we drop the model index $i = 1, 2, …, Q$;

2b) generate the initial ensemble of **Vs*** models using the associated **Vs**^{aux} models as auxiliary variable and conditioning the simulation to the previously generated *Vp* models, so to honour the estimated $p(Vp, Vs)$ distribution. In this case, the Direct Sequential co-simulation algorithm with joint probability distributions [co-DSSj; see Horta and Soares (2010)] and the Bayesian updating strategy (Doyen, 2007) are employed. Note that in this step the γ_{Vs} values are used to compute the autocovariance of the variable to be simulated:

$$C_{Vs^*}(\mathbf{h}) = \gamma_{Vs} \frac{\sigma_{Vs^*}}{\sigma_{Vs^{aux}}} C_{Vp}(\mathbf{h}) = \gamma_{Vs} C_{Vs}(\mathbf{h}) \tag{11}$$

3b) generate the initial ensemble of **ρ*** models with the same strategy previously described in step 2b. The only difference is that, in this simulation, the $\boldsymbol{\rho}^{aux}$ models constitute the auxiliary variable, while the generated density models are conditioned to the previously generated *Vs* models and honour the $p(Vs, \rho)$ distribution;

4b) perform a facies classification based on the previously generated **Vp*** and **Vs*** and $\boldsymbol{\rho}^*$ models and derive the associated *Q* facies models $\boldsymbol{\pi}^*$.

The steps 1b, 2b, 3b, and 4b generate the ensemble of elastic and facies models that constitute the starting points for the geostatistical inversion. However, it is not guaranteed that these models honour the observed seismic data. To this end, this initial population is modified to match the observed seismic response. This updating is performed using an iterative inversion

that is described in the following:

1c) use a seismic forward modelling and a previously determined source wavelet to predict the seismic response associated with the Q $\boldsymbol{\pi}^*$, $\mathbf{Vp}^*$, $\mathbf{Vs}^*$ and $\boldsymbol{\rho}^*$ models. This generates the ensemble of Q predicted seismic data sets $\mathbf{D_{pre}} = \{\mathbf{d}_1^*, \mathbf{d}_2^*, \dots, \mathbf{d}_Q^*\}$. In our case, we employ a convolutional forward modelling based on the full Zoeppritz equations;

2c) each seismic gather (partially stacked data) at each spatial position is compared against the co-located observed data. The comparison is not performed along the entire time axis but within non-overlapping time widows extended over the entire considered angle range. For each j-th predicted gather and for each i-th time window $\mathbf{w}$ we compute the following normalised distance:

$$p_{j,i} = \frac{2c_0(\mathbf{d}_j^*(\mathbf{w}_i), \mathbf{d}(\mathbf{w}_i))}{c_0(\mathbf{d}_j^*(\mathbf{w}_i), \mathbf{d}_j^*(\mathbf{w}_i)) + c_0(\mathbf{d}(\mathbf{w}_i), \mathbf{d}(\mathbf{w}_i))}. \tag{12}$$

For each i-th time window the following objective function is maximised during the geostatistical inversion:

$$\mathbf{E}_{j,i} = \begin{cases} 0 & if \quad p_{j,i} < 0 \\ p_{j,i} & if \quad p_{j,i} \geq 0 \end{cases}, \tag{13}$$

where $c_0(x, y)$ indicates the zero-lag correlation coefficient between the two signals x and y. Note that the $\mathbf{E}_{j,i}$ values lie within [0, 1]. The time length of the windows must be set according to the wavelength period of the source wavelet. For each time window $\mathbf{w}_i$ we extract from the ensemble of Q models the Vp, Vs, and ρ values that generate the best objective function and store these values within the $\mathbf{Vp}^{best}$, $\mathbf{Vs}^{best}$, and $\boldsymbol{\rho}^{best}$, and cubes. Similarly, we store the best objective function value for each time window within the $\boldsymbol{\gamma}^{best}$ cube. The auxiliary volumes $\boldsymbol{\gamma}^{best}$, $\mathbf{Vp}^{best}$, $\mathbf{Vs}^{best}$, and $\boldsymbol{\rho}^{best}$ serve as secondary variables and local regionalised models for the generation of the new set of elastic models for the next iteration. This strategy is similar to that described in Azevedo and Soares (2017), which draw inspiration from the cross-over principle of genetic algorithms. Note that the best Vp, Vs, and ρ cubes, created at the end of each iteration, produce synthetic data with the highest objective function values within each window but are composed by portions of different elastic models. For this reason, these cubes taken together do not honour the assumed spatial correlation model;

3c) update the current $\mathbf{Vp}^*$ models, thus deriving the $\mathbf{Vp}^+$ models with a strategy similar to that used in step 1b, but in this case the $\mathbf{Vp}^{best}$ model is the auxiliary variable, while the correlation coefficients γ_{Vp} for each spatial position are taken from the $\boldsymbol{\gamma}^{best}$ cube. For example, the autocovariance of the variable to be simulated is computed as follows:

$$C_{Vp^+}(\mathbf{h}) = \gamma^{best}(\boldsymbol{\psi_0})C_{Vp}(\mathbf{h}), \tag{14}$$

4c) update the *i*-th **Vs*** model conditioned not only to the best *Vs* model ($\mathbf{Vs}^{best}$), but also to the associated *i*-h **Vp**⁺ model previously created. This is accomplished by the same strategy described in step 2b. The only difference is that $\mathbf{Vs}^{best}$ and γ^{best} are used as auxiliary variables and correlation coefficients to compute the autocovariance. This step provides the **Vs**⁺ models;

5c) a similar approach to that described in the previous step is used to update the *Q* models. These models are conditioned to the previously updated *Vs* models. This step provides the $\boldsymbol{\rho}^{+}$ models;

6c) perform the facies classification on the generated ensemble of $\mathbf{Vp}^{+}$, $\mathbf{Vs}^{+}$ and $\boldsymbol{\rho}^{+}$ models, thus deriving Q updated facies models $\boldsymbol{\pi}^{+}$;

7c) impose $\mathbf{Vp}^{*} = \mathbf{Vp}^{+}$, $\mathbf{Vs}^{*} = \mathbf{Vs}^{+}$, $\boldsymbol{\rho}^{*} = \boldsymbol{\rho}^{+}$, and $\boldsymbol{\pi}^{*} = \boldsymbol{\pi}^{+}$;

8c) iterate from steps 1c to 7c until a maximum number of iterations is reached or when a previously determined average objective function value between observed and predicted data is attained.

The quantification of the uncertainty in seismic inversion is often of crucial importance. For our approach, an exact mathematical assessment of the posterior model is not feasible since we are not sampling the model space according to a Markov Chain Monte Carlo method. However, for an approximated uncertainty quantification and visualisation of the so-called equivalence regions of the solution (Fernandez Martinez, 2012) we can derive the mean predicted model and the associated standard deviation by simply computing the mean and the standard deviation of the elastic $\mathbf{Vp}^{*}$, $\mathbf{Vs}^{*}$and $\boldsymbol{\rho}^{*}$ models generated when the objective function value begin to oscillate around a stable value. With a similar strategy, we can derive the maximum *a-posteriori* (MAP) solution for the facies model and the probability of occurrence of each facies at each spatial location.

We point out that we assume stationary (spatially invariant) variogram model and *a-priori* distribution for the model parameters. More in detail, we consider a Gaussian variogram model along the temporal and spatial directions. However, the implemented approach can easily incorporate facies-dependent spatial correlation patterns and can also be extended to non-stationary variogram models and *a-priori* information. In this case, the entire investigated area should be divided into sub-regions in which the assumption of stationarity is more likely to be valid. Then, the probability distribution and the spatial continuity patterns must be estimated within each zone and the inversion can be run using local multi-distributions and local spatial continuity patterns (Nunes *et al.*, 2017; Sabeti *et al.*, 2017). In the following examples, the temporal correlation function and the *a-priori* model information are calculated from some of the well log data used to generate the true model. Fig. 1 shows a schematic representation of the implemented inversion workflow. Note the different colours that highlight the input for each inversion step. Fig. 2 shows a more detailed representation of the geostatiiled inversion procedure. We implement parallel Matlab codes running on a quad-core Intel i7-7700 at 2.80 GHz with 16 Gb RAM. Due to the limited computational resources available in the following we consider a 2D subsurface model, but the implemented approach is directly extendible to 3D inversions, provided that enough computational resources and efficient inversion codes are available.
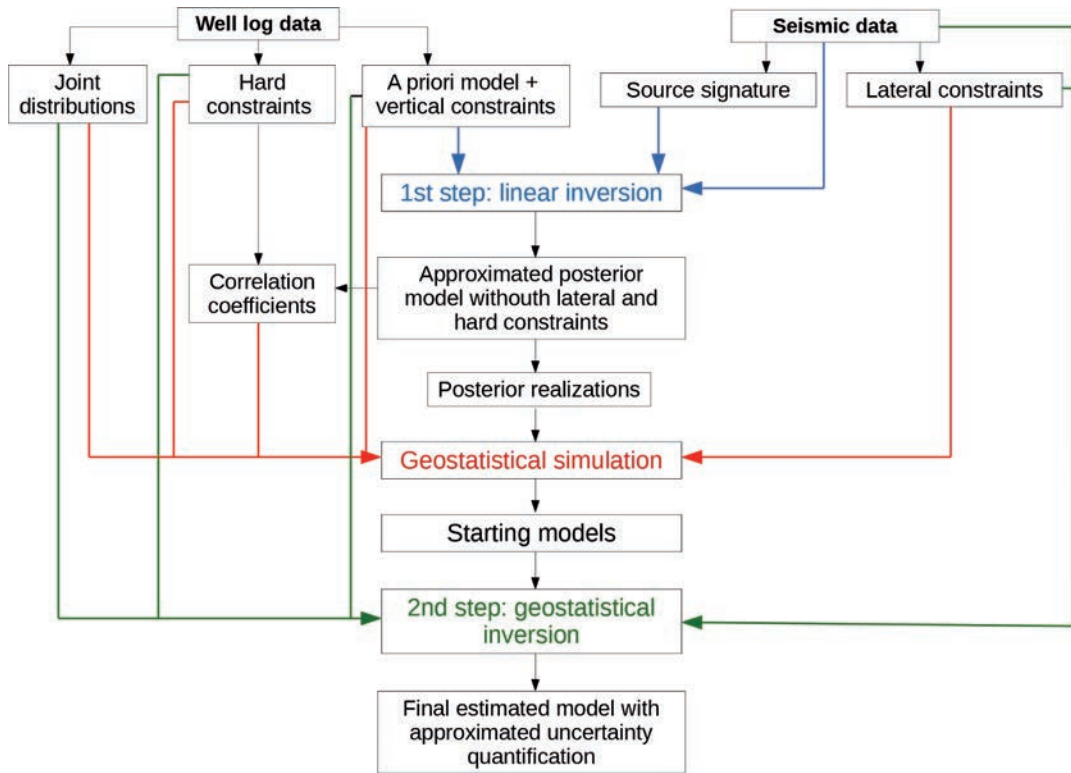
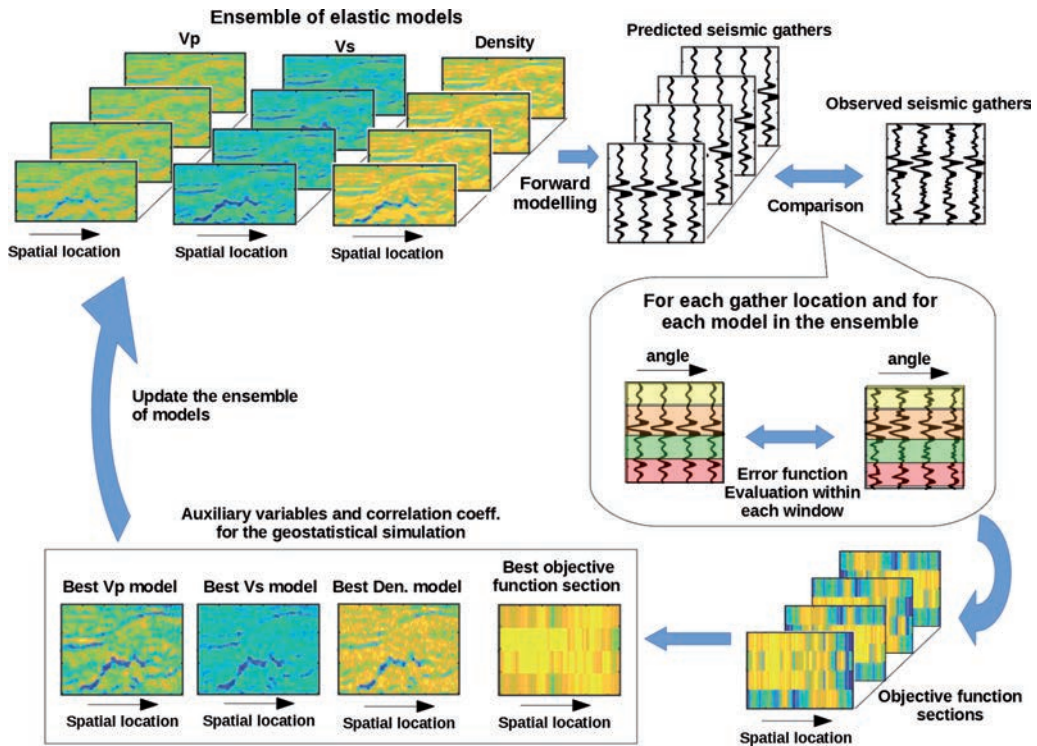Fig. 1 - Schematic workflow of the implemented inversion approach.

Fig. 2 - Schematic workflow of the geostatistical inversion step.

3. Inversion examples

The true model we consider has been derived by integrating a geologic interpretation with the information provided by borehole data pertaining to five wells. This model represents an in-line section extracted from a quite complex geological context where a turbiditic shale-sand sequence hosts gas-saturated sand bodies. 132 time samples and 111 common-mid-point (CMP) gathers form the true model. The time sampling is equal to 0.002 s, whereas 25 m is the distance between each CMP. This translates into a considered time interval of 262 ms and a total profile length of 2750 m. As hard constraints we consider the elastic properties taken at the distance of 1 km. The well log data used to define the true model have also been used to derive the statistical characteristics of the *a-priori* model. In all the following examples, we consider spatially invariant elastic *a-priori* assumptions. Fig. 3 shows the elastic properties of the true model, together with the position of the main gas-saturated sand layer (black arrow), and the spatial position of the hard constraints (red line). In Fig. 3 the low *Vp*, *Vs,* and ρ values identify the sand bodies, while shales are characterised by higher elastic property values. Note, that the shale and sand formations are characterised by spatially variant orientations and relationships. For the inversion, we consider three facies: shale, brine sand, and gas sand.
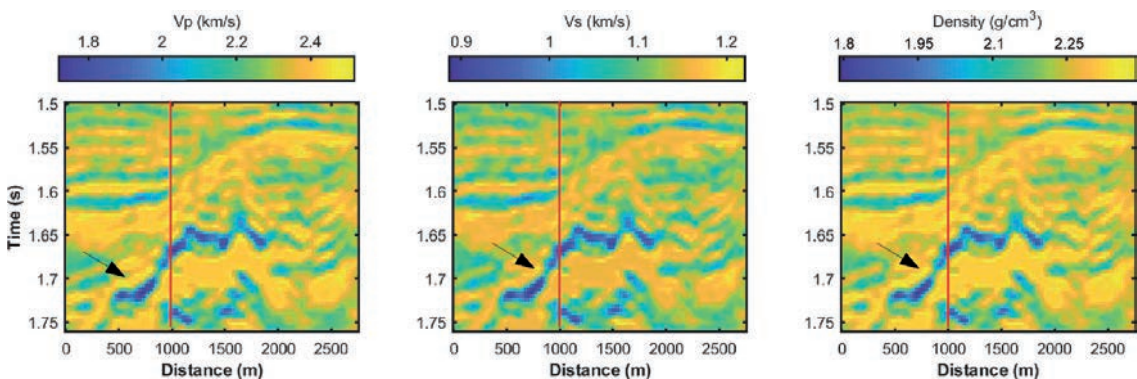
Fig. 3 - From left, to right we represent the true *Vp*, *Vs,* and ρ models. The dashed red line represents the assumed position of the well that constitutes the hard constraints, whereas the black arrows indicate the main sand body target of the inversion process.

Fig. 4 represents the joint distribution of the elastic properties projected onto the *Vp-Vs* and *Vp-ρ* planes. These distributions have been estimated by applying the kernel density estimation algorithm (with a Gaussian kernel) to the ensemble of available well log data. The distributions of Fig. 4 have been used in the Bayesian updating step of the co-simulation procedure. Note the non-linearity of the *Vp-Vs* and of the *Vp-ρ* relations indicating that, in this case, the use of a simple collocated cokriging approach, assuming a linear relationship between the auxiliary variable and the variable to be simulated, would have provided simulated properties with spurious mutual correlations. Instead, the use of the Bayesian updating approach with the joint distribution guarantees the actual distribution of the elastic properties being preserved during the simulation process.

Fig. 5 represents the distribution of the elastic parameters within each facies projected (for graphical convenience) onto the P-impedance, S-impedance (*Ip-Is*) plane. Again, this distribution
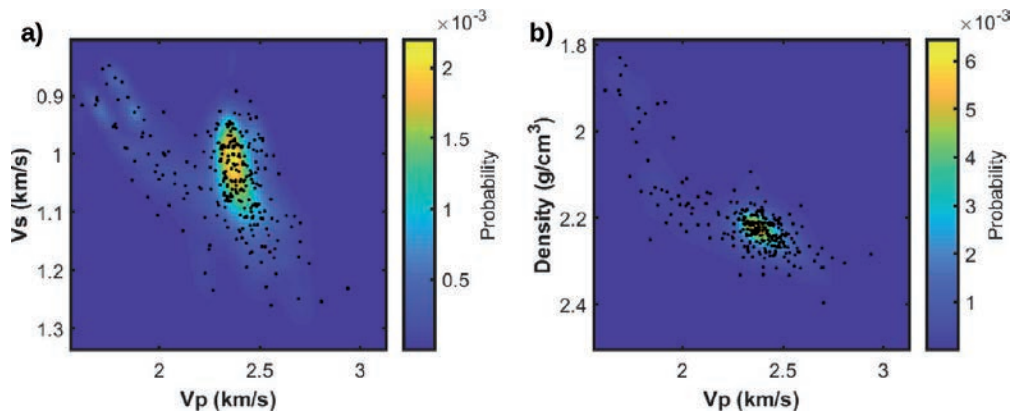
Fig. 4 - Joint distributions of *Vp-Vs,* and *Vp-ρ* (panels a and b, respectively). The black circles represent the well log data input to the kernel density estimation, whereas the colour maps code the probability values.
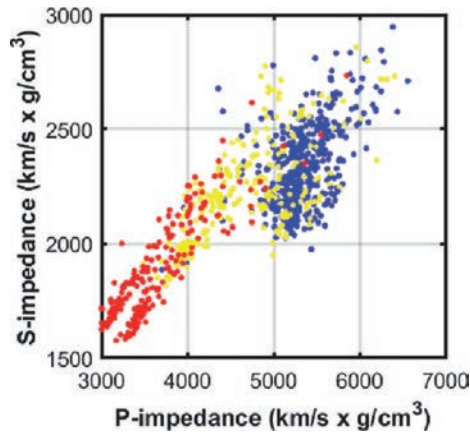

Fig. 5 - Distribution of the elastic properties of *Ip* and *Is* within each facies derived from the available well log data. Blue, yellow, and red represent shale, brine sand, and gas sand, respectively.

has been derived from the available well log data and has been used to derive the statistical properties of the facies-dependent prior model and to train the Bayes classification algorithm. As expected, we observe that the *Ip* and *Is* values decrease passing from shale to sand and when gas replaces brine in the pore space.

Fig. 6 illustrates the 1D marginal non-parametric *a-priori* distributions used in the geostatistical inversion and derived by applying the kernel density estimation method to the available well log information. In each facies component, we note multimodalities and skewness that indicate the deviation of the actual distributions from a simple Gaussian model. However, in the first analytical inversion step, we neglect these deviations by simply assuming Gaussian-distributed elastic parameters within each facies (Fig. 6). The prior weights and the statistical properties of the mixture have been derived using the expectation-maximisation method applied to the ensemble of available well log information (Hastie *et al.*, 2005). Note that the *Vp*, *Vs*, and *ρ* values show an overall decrease moving from shale to brine sand and gas sand and that shale is expected to be the most probable facies in the investigated area (i.e. the facies with the highest prior weights).
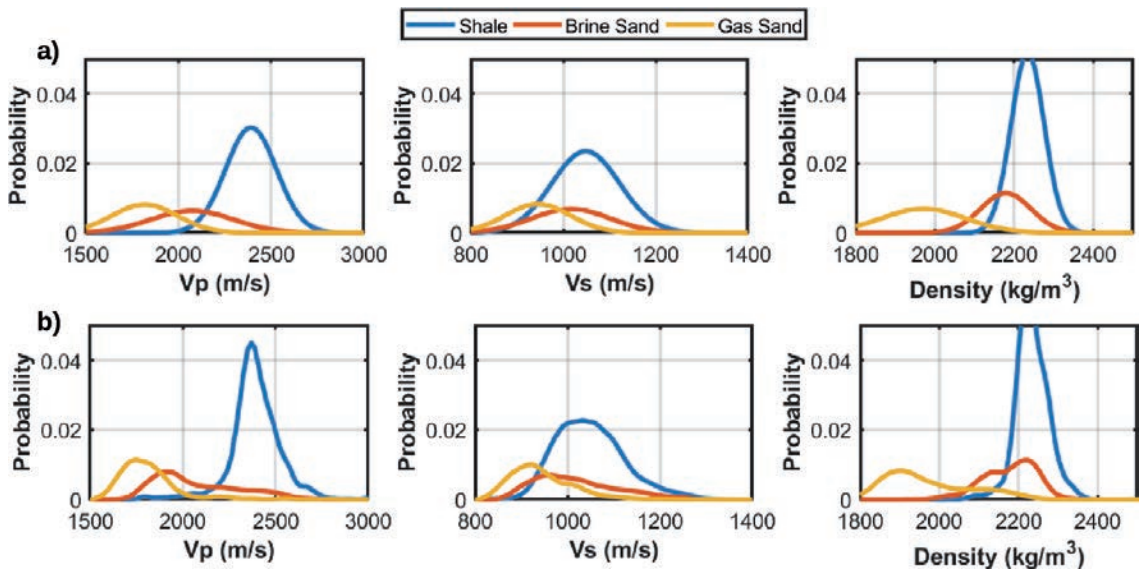
Fig. 6 - Gaussian-mixture marginal priors employed in the first analytical inversion step (a) and the 1D marginal prior distributions showing the three components of the non-parametric distributions derived from the available well log data and employed in the geostatistical inversion step (b).

Fig. 7 shows the experimental and modelled temporal and spatial correlation functions. The experimental temporal correlation function has been derived from the available well log data, whereas the lateral variability of the observed seismic data has been used to calibrate the spatial correlation pattern. For simplicity, we consider a stationary correlation function equal for all the considered litho-fluid classes. However, if needed a facies-dependent correlation can be used to properly model the different lateral and vertical variability of the elastic properties within each facies.
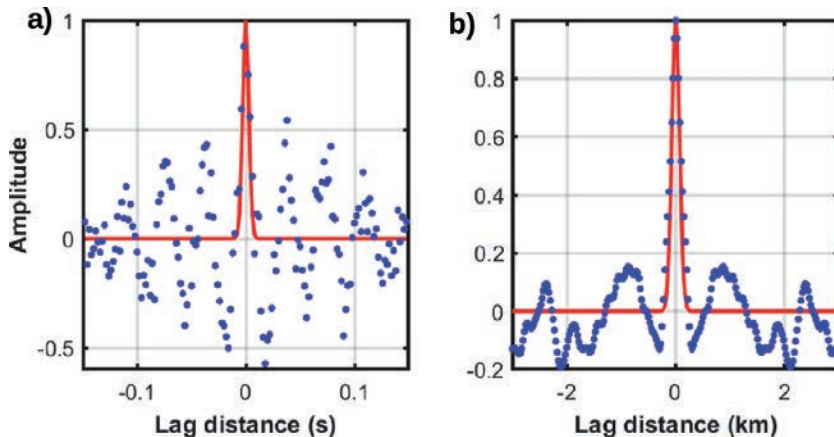
Fig. 7 - Experimental (blue circles) and modelled (red curve) temporal correlation functions (a). The blue circles represent the average temporal autocorrelation of the available well log data. The red curve represents the temporal constraints included in the first and second steps of the inversion procedure. The modelled correlation corresponds to a Gaussian variogram model with a range of 6 ms. Experimental (blue circles) and assumed (red curve) spatial correlation function (b). The blue circles represent the average spatial autocorrelation of the observed seismic data. The red curve represents the spatial constraints included in the second step of the inversion procedure. The modelled correlation corresponds to a Gaussian variogram model with a range of 90 m.

To demonstrate the applicability and the benefits of the implemented inversion approach over a more standard linear inversion, we perform two different inversion experiments with different signal-to-noise (S/N) ratios in the data. In both cases, we assume Gaussian distributed random noise and the observed data have been computed using a 1D convolutional forward operator based on the full Zoeppritz equations and for the incidence angles of 0, 15, and 30 degrees, while a 50-Hz zero-phase Ricker constitutes the source wavelet. In the first example, the observed data are characterised by a high S/N ratio equal to 25 (computed as the ratio of the summed squared magnitude of the noise-free data to that of the noise vector). In the second case, the S/N ratio is equal to 2. In both tests, we assume that the source wavelet is perfectly known, although this is a simplification with respect to real data applications in which the estimated wavelet is usually affected by errors and uncertainties.

We now describe the first test in which the observed data are characterised by high S/N ratio. Fig. 8a compares the true facies model and the MAP facies solution provided by the first linear inversion step. In this favourable scenario, the linear inversion yields satisfactory results in which the actual facies model is accurately predicted. Fig. 8b shows the mean posterior elastic model estimated by the first step of linear inversion. Again, we observe final predictions in good agreement with the true properties that satisfactory preserve the actual spatial continuity of the elastic parameters. Fig. 9 shows direct comparisons between the elastic properties that constitute the assumed hard constraints and the co-located mean *a-posteriori* model estimated by the first inversion step. We obtain very high correlation coefficients between the true and the predicted model that, as expected, decrease from *Vp* (the best resolved elastic parameter) to *Vs* and ρ (the least resolvable property). These coefficients are used as correlation values in
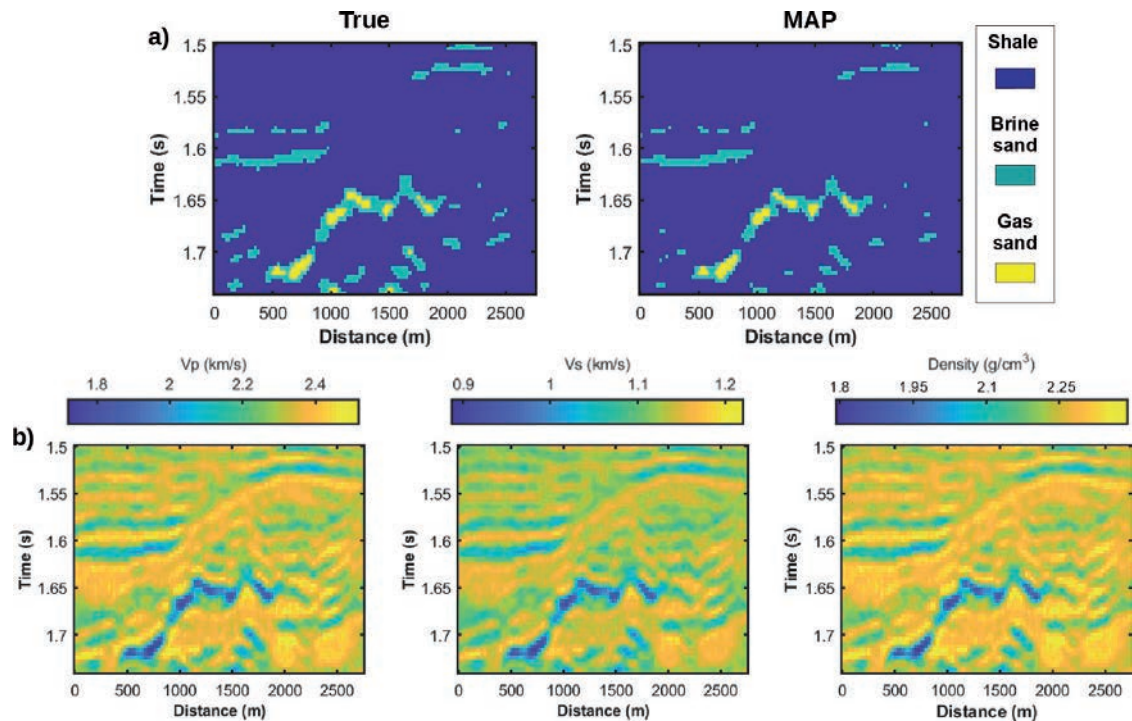

Fig. 8 - Inversion results after the first step for a S/N ratio equal to 25: a) comparison between the true facies models and the MAP facies solution; b) mean *a-posteriori Vp*, *Vs,* and *p* models.
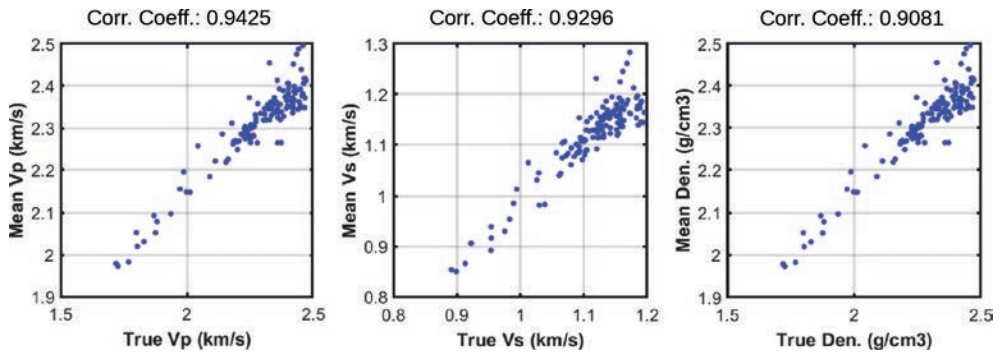
Fig. 9 - Cross-plots between the hard constraints and the co-located mean *Vp*, *Vs,* and ρ models estimated by the first step of linear inversion.

the geostatistical simulation process that generates the ensemble of starting models for the second inversion step. Fig. 10 illustrates 4 out of the 10 models forming the initial population input to the geostatistical inversion. The difference between the models represented in Fig. 8 and those displayed in Fig. 10 is that the former are predictions of a linear inversion without the inclusion of hard and lateral constraints. Instead, the latter results from a geostatistical simulation process that imposes hard and lateral constraints to the outcomes of the linear inversion. However, these starting models are not directly constrained by the seismic data and
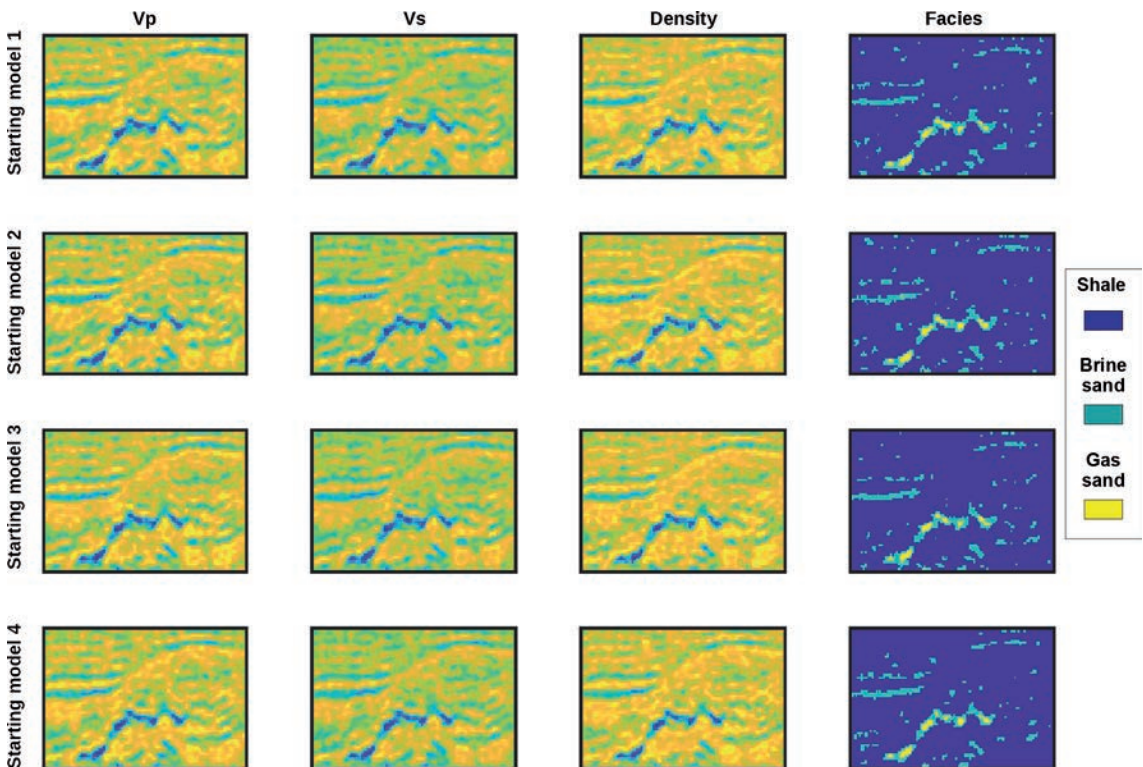
Fig. 10 - From top to bottom we represent 4 out of the 10 starting models used in the geostatistical inversion.

for this reason, they must be refined and updated during the geostatistical inversion. In all the following examples the second step of geostatistical inversion runs for 40 iterations and makes use of the exact Zoeppritz equations as the forward modelling. Note that the use of the exact Zoeppritz equations makes it possible to extend the incidence angle range with respect to that considered in the first step of linear inversion. However, for the sake of coherency, in all the following tests the incidence angle range is always limited to the three angle stacks of 0, 15, and 30 degrees.

Fig. 11 shows the evolution of the correlation coefficient between the observed data and the data predicted by the ensemble mean model provided by the geostatistical inversion. We observe that the algorithm reaches convergence just after 5 iterations after which the correlation value starts to oscillate around a stable value. This indicates that the convergence is achieved in 5 iterations, and hence all the models generated after the fifth iteration have been used to compute the final average Vp, Vs, and ρ sections and the associated standard deviation values.

Fig. 12 represents the mean Vp, Vs, and ρ models estimated at the end of the geostatistical inversion. The good agreement between these estimations and the true model demonstrates
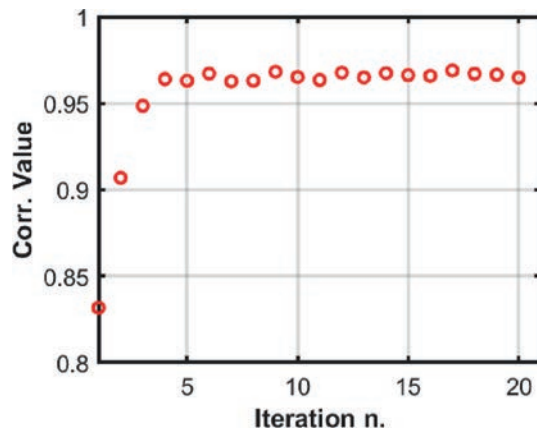

Fig. 11 - Evolution for the first 20 iterations of the correlation coefficient between the observed data and the data predicted on the average ensemble model estimated at each iteration.
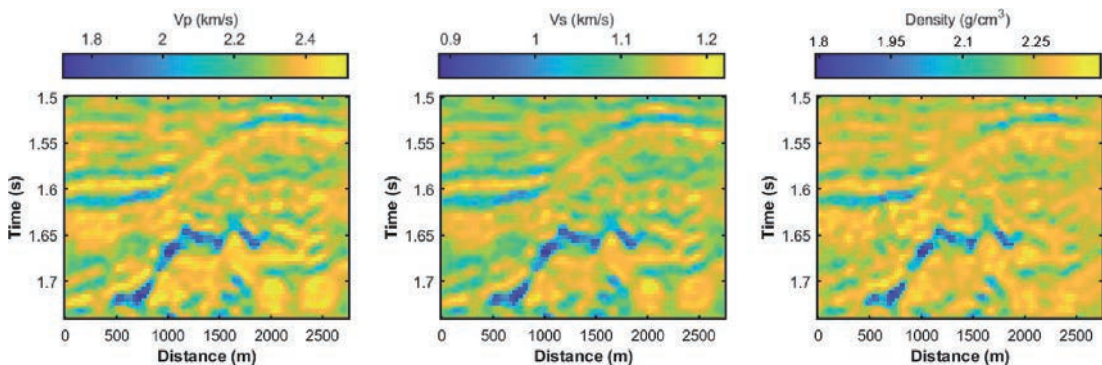

Fig. 12 - Final mean Vp, Vs, and ρ models predicted at the end of the second step of geostatistical inversion.

the reliability of the implemented inversion approach. Fig. 13a confirms that the litho-fluid classes have been correctly identified, and particularly the gas-saturated sand bodies have been located with very low ambiguity (Fig. 13b). To better quantify the improvement on the facies classification at the end of the geostatistical inversion with respect to the predictions of the linear inversion, we compute the so-called confusion matrices between the true facies model and the MAP facies solutions retrieved by the two inversion steps (Fig. 14). The diagonal elements of these matrices quantify the percentage of samples actually belonging to each facies that have been correctly classified in that facies, while the off-diagonal elements indicate misclassifications. After both the first and second inversion step almost the 100% of shales have been correctly identified, while the second step of geostatistical inversion results
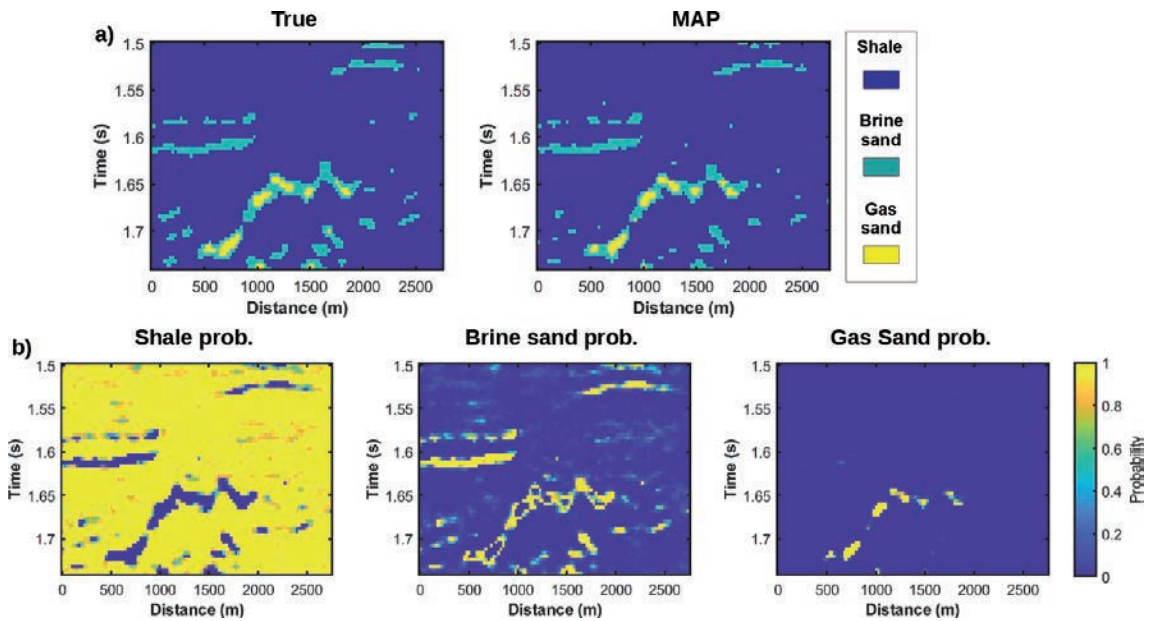

Fig. 13 - Comparison of the true facies model and the MAP facies solution retrieved by the geostatistical inversion (a) and probability of occurrence of each facies at each spatial location as estimated by the geostatistical inversion (b).
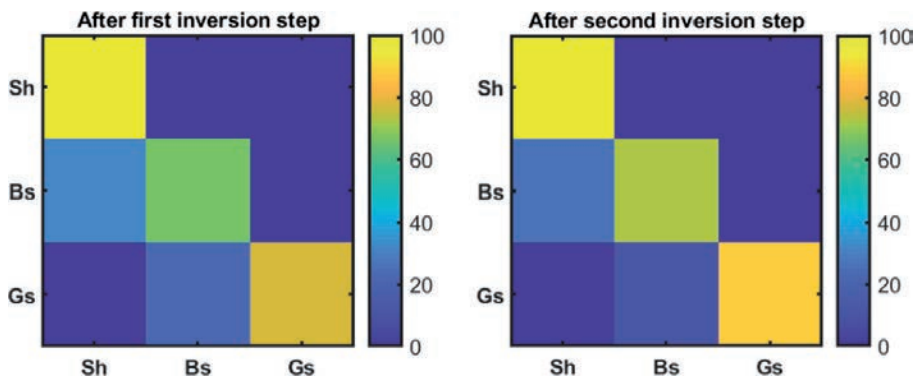

Fig. 14 - Confusion matrices computed by comparing the true facies model and the MAP facies solution estimated by the linear inversion (left) and the geostatistical inversion (right). Sh, Bs and Gs refer to shale, brine sand and gas sand, respectively.

in a slight improvement of the gas sand classification. The off-diagonal values indicate that both inversion steps interpreted some brine sand bodies as shale, whereas some gas sands have been erroneously attributed to brine sands.

We now repeat the inversion for the data set with the S/N ratio equal to 2. Fig. 15a shows that in this case the MAP facies solution estimated by the linear inversion overpredicts the occurrence of brine sand, and none of the gas sands have been correctly identified. In the predicted facies model the main sand bodies object of this study is characterised by a poor spatial continuity, and this makes the mapping of the sand boundaries ambiguous. The *a-posteriori* mean *Vp*, *Vs*, and ρ models (Fig. 15b) clearly show lateral scattering resulting from the error propagation from the data to the model space. In this context, the inclusion of lateral constraints is particularly useful to promote the spatial continuity of the predicted continuous and discrete properties. In Fig. 15b also note the overall underestimation of the elastic contrasts at the reflecting interfaces. Indeed, in this case with significant noise contamination, the data covariance matrix indicates that we are less confident on the observed data and for this reason the Bayesian inversion is mainly driven by the spatially invariant and constant *a-priori* elastic model.
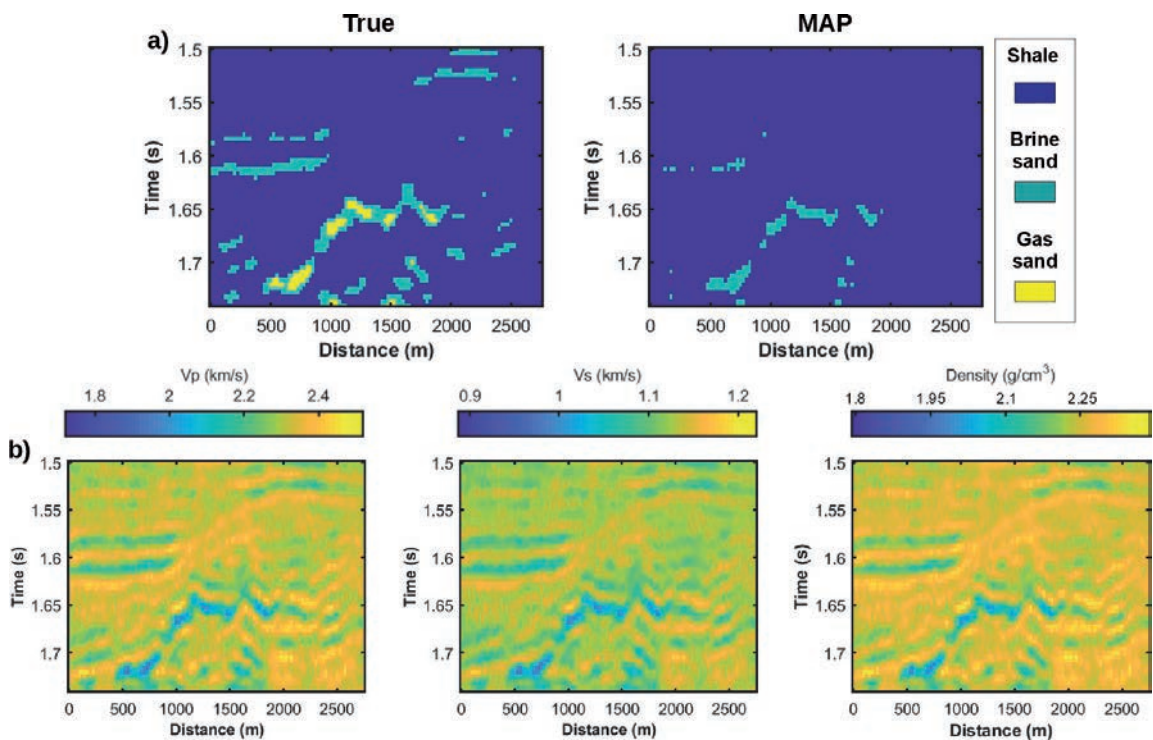

Fig. 15 - Inversion results after the first step for a S/N ratio equal to 2: a) comparison between the true facies models and the MAP facies solution; b) mean *a-posteriori Vp*, *Vs*, and ρ models.

Similar to the previous test, we run the geostatistical inversion for 40 iterations using an initial ensemble of 10 *Vp*, *Vs,* and ρ models. In Fig. 16 we observe that the correlation value between observed data and the data predicted on the ensemble average stabilises after five iterations. Therefore, all the elastic and facies models generated after the first five iterations have been used to compute the final predictions (mean elastic model and MAP
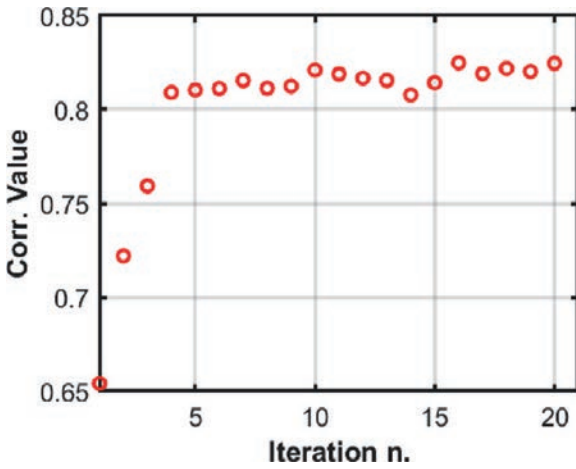
Fig. 16 - Evolution for the first 20 iterations of the correlation coefficient between the observed data and the data predicted on the mean ensemble model estimated at each iteration.
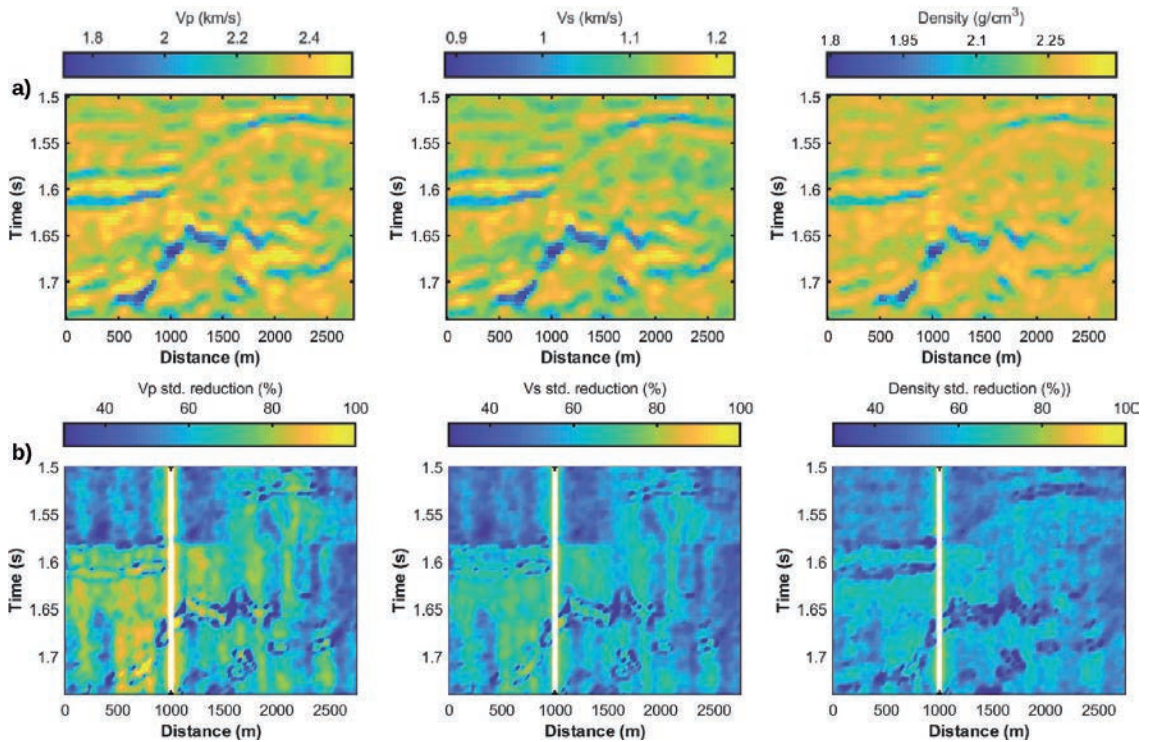

Fig. 17 - Final mean models predicted at the end of the second step of geostatistical inversion (a) and percentage reduction of the posterior uncertainty with respect to the *a-priori* uncertainty (b).

facies solution) and the associated uncertainties. The final mean elastic models predicted by the geostatistical inversion are illustrated in Fig. 17a. We note that the lateral and hard constraints infused into the geostatistical inversion significantly reduce the lateral scattering that affected the outcomes of the first inversion step. Besides, by comparing the true model of Fig. 3 with those shown in Figs. 15b and 17a, we can appreciate how the geostatistical
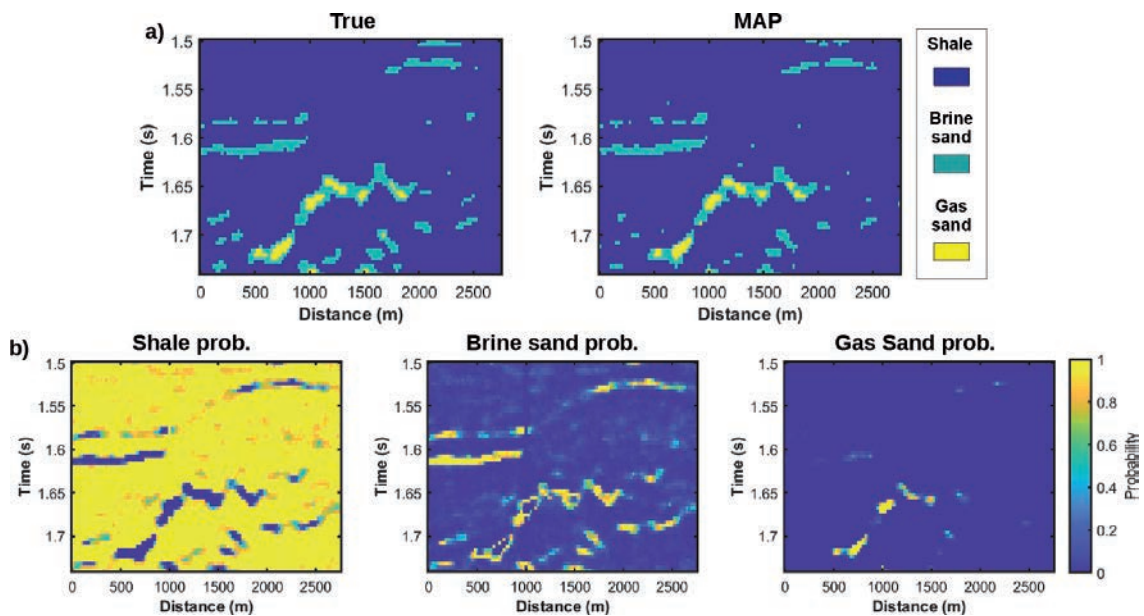
Fig. 18 - Comparison of the true facies model and the MAP facies solution retrieved by the geostatistical inversion (a) and probability of occurrence of each facies at each spatial location as estimated by the geostatistical inversion (b).

inversion moves the Vp, Vs, and ρ predictions very close to the true model even in this non-favourable scenario characterised by a low S/N ratio. Fig. 17b represents the percentage reduction of the posterior uncertainty on the estimated elastic parameters with respect to the *a-priori* uncertainty. As expected, the uncertainty reduction is higher for Vp and lower for density. In Fig. 18 we observe the close match between the true facies model and the MAP facies solution recovered by the geostatistical inversion. The improvements in the facies prediction achieved by the second inversion step can be appreciated by comparing Fig. 18a with Fig. 15a. The increased spatial continuity of the results achieved by the geostatistical inversion facilitates the mapping of the sand bodies throughout the inverted section. Figs. 19 and 20 show a comparison between the observed partial angle stacks at 0, 15 and 30 degrees and the stacks computed on the mean models estimated after the first and second inversion step, respectively. In Fig. 19 we observe that the lateral scattering affecting the estimated elastic models generates lateral scattering also on the estimated partially stacked sections. This lateral scattering is efficiently attenuated by the geostatistical inversion (Fig. 20). The underpredictions of the seismic amplitudes visible in the rightmost plots of Fig. 19 are related to the overall underpredictions of the elastic property contrasts at the interfaces (Fig. 15b). A comparison of Figs. 19 and 20 also illustrates the overall decrease of the data misfit as we pass from the first to the second inversion step. Finally, the comparison of the confusion matrices computed after the first and second estimation steps (Fig. 21) highlights the improvements in the facies classification achieved by the geostatistical inversion. After the second step, 100% of the shales and more than 60% of brine and gas sands have been correctly identified. Differently after the linear inversion only 25% of gas sands and 0% of gas sands were correctly classified, while 75% of brine sands were interpreted as shales, 92% of gas sands were erroneously classified as brine saturated, and 8% of gas sands were classified as shales.
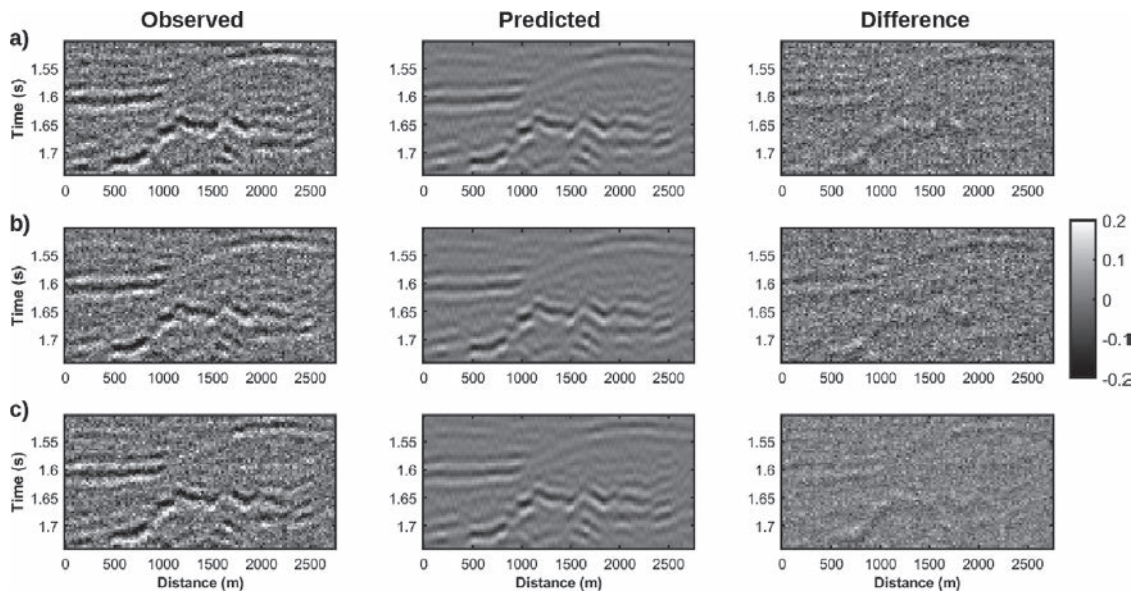
Fig. 19 - Comparison between the observed angle stacks (left), the predicted angle stacks computed on the mean *a-posteriori* model (centre) provided by the first inversion step, and their difference (right): a) angle stacks for an incidence angle of 0°; b) angle stacks for an incidence angle of 15°; c) angle stacks for an incidence angle of 30°.
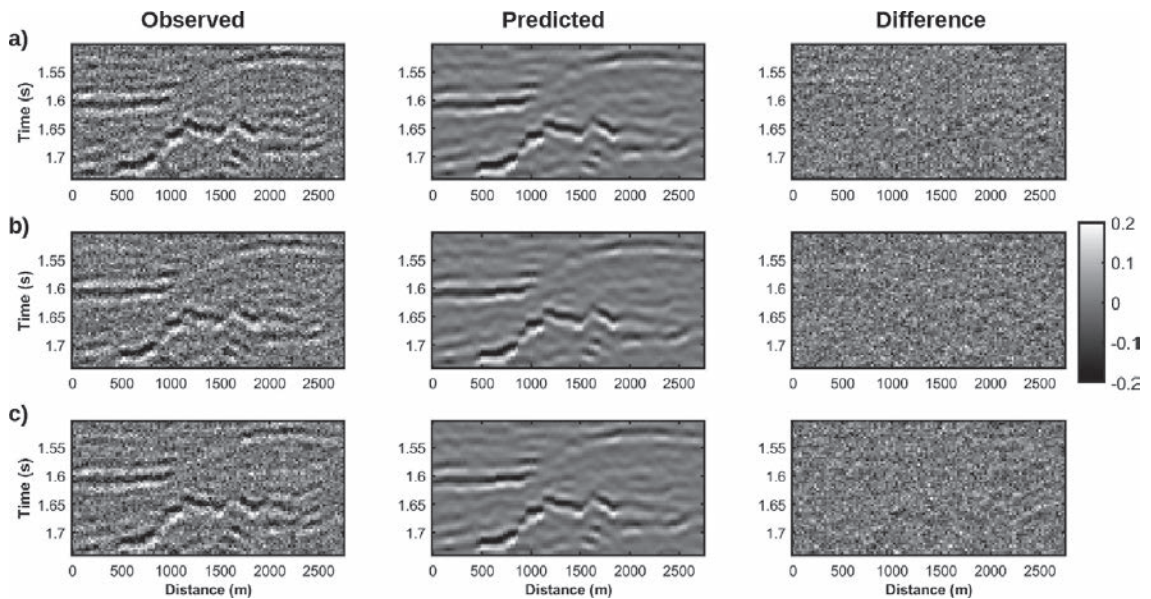

Fig. 20 - Comparison between the observed angle stacks (left), the predicted angle stacks computed on the mean model estimated by the second inversion step (centre), and their difference (right): a) angle stacks for an incidence angle of 0°; b) angle stacks for an incidence angle of 15°; c) angle stacks for an incidence angle of 30°.
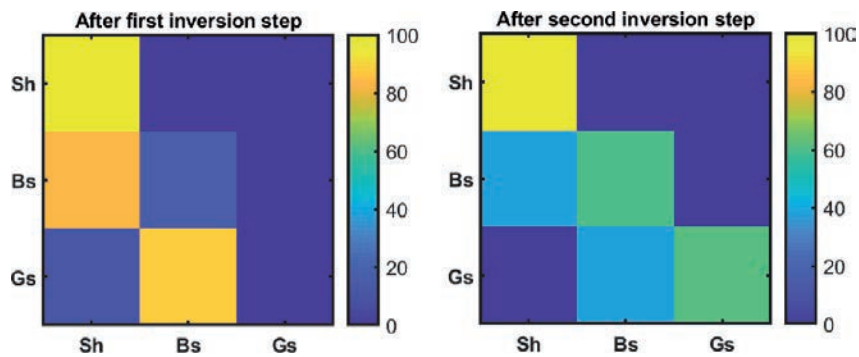
Fig. 21 - Confusion matrices computed by comparing the true facies model and the MAP facies solution retrieved by the linear inversion (left) and the geostatistical inversion (right). Sh, Bs and Gs refer to shale, brine sand and gas sand, respectively.

4. Conclusions

We described an inversion approach that infers discrete (litho-fluid classes) and continuous (Vp, Vs, and ρ properties from pre-stack seismic data. The implemented inversion is primarily devoted at attenuating the noise propagation from the data to the model space in case of low-quality seismic gathers so to achieve more stable and spatially continuous estimations of the sough subsurface characteristics. The inclusions of hard and spatial constraints into the inversion framework usually results in a substantial increase in the computational cost of the estimation process. For this reason, we split the whole inversion process into two cascade steps. The first one is a computationally fast linear Bayesian inversion that converts the pre-stack data into the elastic properties. The use of a linear or linearised forward modelling operator, and the assumption of a Gaussian-mixture prior model allows for an analytical and exact assessment of the posterior uncertainty for both the discrete and the continuous property. To limit the computational effort, this first step separately inverts each seismic gather and only impose vertical constraints to the recovered solution. The second step of geostatistical inversion is aimed at refining the outcomes of the previous step by adding the available hard constraints, and by imposing a lateral continuity pattern to the recovered model. Starting the geostatistical inversion from an ensemble of models that already quite accurately reproduce the observed data reduces the computational costs of the geostatistical inversion procedure, that is a lower number of generated models (and forward modelling evaluations) are needed to attain convergence. Moreover, this second inversion step relaxes the need of a linear forward operator and the assumption of an analytic prior model and it can also incorporate a non-linear seismic forward modelling (e.g. the Zoeppritz equations). All the models generated during the second inversion step reproduce the available hard constraints, the prior assumptions, and the spatial variogram model as estimated from the available well log data. In the second step, the Bayesian approach has been used to perform the facies classification on each generated model, but, if needed, any other classification method can be incorporated into the inversion framework. The ensemble of models generated during the geostatistical inversion can be used to numerically compute an approximated uncertainty quantification. A Markov Chain Monte Carlo sampling could be used for an accurate uncertainty assessment, but at the expense of a substantial increase of the computational effort. We implement parallel Matlab inversion codes running on a notebook

equipped with an Intel i7-7700 at 2.80 GHz with 16 Gb RAM. The parallelisation is particularly useful to speed up the geostatistical inversion because the generation and the update of the ensemble of models at each iteration can be easily distributed across different cores. All the described examples run in 90 minutes, approximately. For the limited computational resources available, we focused the attention to 2D models, but the method can be also applied to 3D inversions. To this end, a more efficient and scalable inversion code is needed.

REFERENCES

Aki K. and Richards P.G.; 1980: *Quantitative seismology: theory and methods, Vols. I and II*. W.H. Freeman, San Francisco, CA, USA, 573 + 391 pp.

Aleardi M.; 2015: *The importance of the Vp/Vs ratio in determining the error propagation, the stability and the resolution of linear AVA inversion: a theoretical demonstration*. Boll. Geof. Teor. Appl., 56, 357-366.

Aleardi M. and Salusti A.; 2019: *Markov chain Monte Carlo algori thms for target-oriented and interval-oriented amplitude versus angle inversions with non-parametric priors and non-linear forward modellings*. Geophys. Prospect., 68, 735-760, doi: 10.1111/1365-2478.12876.

Aleardi M., Mazzotti A., Tognarelli A., Ciuffi S. and Casini M.; 2015: *Seismic and well log characterization of fractures for geothermal exploration in hard rocks*. Geophys. J. Int., 203, 270-283.

Aleardi M., Ciabarri F. and Gukov T.; 2018: *A two-step inversion approach for seismic-reservoir characterization and a comparison with a single-loop Markov-chain Monte Carlo algorithm*. Geophys., 83, R227-R244.

Aleardi M., Ciabarri F. and Gukov T.; 2019: *Reservoir characterization through target-oriented AVA-petrophysical inversions with spatial constraints*. Pure Appl. Geophys., 176, 901-924.

Alemie W. and Sacchi M.D.; 2011: *High-resolution three-term AVO inversion by means of a Trivariate Cauchy probability distribution*. Geophys., 76, R43-R55.

Aster R.C., Borchers B. and Thurber C.H.; 2018: *Parameter estimation and inverse problems, 3rd ed*. Elsevier, Amsterdam, The Netherlands, 404 pp.

Azevedo L. and Soares A.; 2017: *Geostatistical methods for reservoir geophysics*. Springer International Publishing, Berlin, Germany, 168 pp., doi: 10.1007/978-3-319-53201-1.

Bongajum E.L., Boisvert J. and Sacchi M.D.; 2013: *Bayesian linearized seismic inversion with locally varying spatial anisotropy*. J. Appl. Geophys., 88, 31-41.

Bortoli L.J., Alabert F., Haas A. and Journel A.; 1993: *Constraining stochastic images to seismic data*. In: Soares A. (ed), Geostatistics Tróia '92, Quantitative Geology and Geostatistics, Springer, Dordrecht, The Netherlands, Vol. 5, pp. 325-337, doi: 10.1007/978-94-011-1739-5_27.

Bosch M., Carvajal C., Rodrigues J., Torres A., Aldana M. and Sierra J.; 2009: *Petrophysical seismic inversion conditioned to well-log data: methods and application to a gas reservoir*. Geophys., 74, O1-O15.

Bosch M., Mukerji T. and Gonzalez E.F.; 2010: *Seismic inversion for reservoir properties combining statistical rock physics and geostatistics: a review*. Geophys., 75, 75A165-75A176.

Buland A. and Omre H.; 2003: *Bayesian linearized AVO inversion*. Geophys., 68, 185-198.

de Figueiredo L.P., Grana D., Bordignon F.L., Santos M., Roisenberg M. and Rodrigues B.B.; 2018: *Joint Bayesian inversion based on rock-physics prior modeling for the estimation of spatially correlated reservoir properties*. Geophys., 83, M49-M61.

Doyen P.; 2007: *Seismic reservoir characterization: an earth modelling perspective (EET 2)*. EAGE publications, Houten, The Netherlands, 255 pp.

Fernandez Martinez J.L., Fernandez Muniz M.Z. and Tompkins M.J.; 2012: *On the topography of the cost functional in linear and nonlinear inverse problems*. Geophys., 77, W1-W15.

Gunning J. and Sams M.; 2018: *Joint facies and rock properties Bayesian amplitude-versus-offset inversion using Markov random fields*. Geophys. Prospect., 66, 904-919.

Haas A. and Dubrule O.; 1994: *Geostatistical inversion-a sequential method of stochastic reservoir modelling constrained by seismic data*. First break, 12, 561-569.

Hastie T., Tibshirani R., Friedman J. and Franklin J.; 2005: *The elements of statistical learning: data mining, inference and prediction*. Math. Intell., 27, 83-85.

Horta A. and Soares A.; 2010: *Direct sequential co-simulation with joint probability distributions*. Math. Geosci., 42, 269-292.

Laloy E., Hérault R., Jacques D. and Linde N.; 2018: *Training-image based geostatistical inversion using a spatial generative adversarial neural network*. Water Resour. Res., 54, 381-406.

Menke W.; 2018: *Geophysical data analysis: discrete inverse theory, 4th ed.* Academic Press, Elsevier, Amsterdam, The Netherlands, 352 pp.

Nunes R., Soares A., Azevedo L. and Pereira P.; 2017: *Geostatistical seismic inversion with direct sequential simulation and co-simulation with multi-local distribution functions*. Math. Geosci., 49, 583-601.

Sabeti H., Moradzadeh A., Ardejani F.D., Azevedo L., Soares A., Pereira P. and Nunes R.; 2017: *Geostatistical seismic inversion for non-stationary patterns using direct sequential simulation and co-simulation*. Geophys. Prospect., 65, 25-48.

Sarma D.D.; 2010: *Geostatistics with applications in Earth sciences, 2nd ed*. Springer, Dordrecht, The Netherlands, 222 pp., doi: 10.1007/978-1-4020-9380-7.

She B., Wang Y., Liang J., Liu Z., Song C. and Hu, G.; 2018: *A data-driven amplitude variation with offset inversion method via learned dictionaries and sparse representation*. Geophysics, 83(6), R725-R748.

Soares A.; 2001: *Direct sequential simulation and cosimulation*. Mathematical Geology, 33(8), 911-926.

Tarantola A.; 2005: *Inverse problem theory and methods for model parameter estimation*. Society for Industrial and Applied Mathematics, Philadelphia, PA, USA, 348 pp., doi: 10.1137/1.9780898717921.

Tetyukhina D., van Vliet L.J., Luthi S.M. and Wapenaar K.; 2010: *High-resolution reservoir characterization by an acoustic impedance inversion of a Tertiary deltaic clinoform system in the North Sea*. Geophys., 75, O57-O67.

Theune U., Jensås I.Ø. and Eidsvik J.; 2010: *Analysis of prior models for a blocky inversion of seismic AVA data*. Geophys., 75, C25-C35.

Ulvmoen M., Omre H. and Buland A.; 2010: *Improved resolution in Bayesian lithology/fluid inversion from prestack seismic data and well observations: part 2-real case study*. Geophys., 75, B73-B82.

Wang R. and Wang Y.; 2016: *Multichannel algorithms for seismic reflectivity inversion*. J. Geophys. Eng., 14, 41.

Xu W., Tran T.T., Srivastava R.M. and Journel A.G.; 1992: *Integrating seismic data in reservoir modeling: the collocated cokriging alternative*. In: Proc., Annual Technical Conference and Exhibition, Society of Petroleum Engineers, Washington, D.C., USA, SPE-24742-MS, doi: 10.2118/24742-MS.

Zunino A., Mosegaard K., Lange K., Melnikova Y. and Mejer Hansen T.; 2015: *Monte Carlo reservoir analysis combining seismic reflection data and informed priors*. Geophys., 80, R31-R41.

Corresponding author: Mattia Aleardi
                            Earth Sciences Department, University of Pisa
                            Via S. Maria 53, 56126 Pisa, Italy
                            Phone: +39 050 2215722; e-mail: mattia.aleardi@unipi.it